

## EXPLORING THE VARIABLE SKY WITH LINEAR. I. PHOTOMETRIC RECALIBRATION WITH THE SLOAN DIGITAL SKY SURVEY

BRANIMIR SESAR<sup>1,2</sup>, J. SCOTT STUART<sup>3</sup>, ŽELJKO IVEZIĆ<sup>2</sup>, DYLAN P. MORGAN<sup>2,4</sup>,

ANDREW C. BECKER<sup>2</sup>, AND PRZEMYSŁAW WOŹNIAK<sup>5</sup>

<sup>1</sup> Division of Physics, Mathematics and Astronomy, Caltech, Pasadena, CA 91125, USA

<sup>2</sup> Department of Astronomy, University of Washington, Seattle, WA 98195-1580, USA

<sup>3</sup> Lincoln Laboratory, Massachusetts Institute of Technology, Lexington, MA 02420-9108, USA

<sup>4</sup> Department of Astronomy, Boston University, Boston, MA 02139, USA

<sup>5</sup> Los Alamos National Laboratory, Los Alamos, NM 87545-0001, USA

Received 2011 July 13; accepted 2011 September 23; published 2011 November 4

### ABSTRACT

We describe photometric recalibration of data obtained by the asteroid survey LINEAR. Although LINEAR was designed for astrometric discovery of moving objects, the data set described here contains over 5 billion photometric measurements for about 25 million objects, mostly stars. We use Sloan Digital Sky Survey (SDSS) data from the overlapping  $\sim 10,000 \text{ deg}^2$  of sky to recalibrate LINEAR photometry and achieve errors of 0.03 mag for sources not limited by photon statistics with errors of 0.2 mag at  $r \sim 18$ . With its 200 observations per object on average, LINEAR data provide time domain information for the brightest four magnitudes of the SDSS survey. At the same time, LINEAR extends the deepest similar wide-area variability survey, the Northern Sky Variability Survey, by 3 mag. We briefly discuss the properties of about 7000 visually confirmed periodic variables, dominated by roughly equal fractions of RR Lyrae stars and eclipsing binary stars, and analyze their distribution in optical and infrared color–color diagrams. The LINEAR data set is publicly available from the SkyDOT Web site.

**Key words:** binaries: eclipsing – catalogs – stars: variables: general – stars: variables: RR Lyrae – surveys

**Online-only material:** color figures

### 1. INTRODUCTION

Variability is an important phenomenon in astrophysical studies of structure and evolution, both stellar and Galactic and extragalactic. Some variable stars, such as RR Lyrae stars, are an excellent tool for studying the Galaxy. Being nearly standard candles (thus making distance determination relatively straightforward) and being intrinsically bright, they are a particularly suitable tracer of Galactic structure (e.g., Sesar et al. 2007, and references therein). Similarly, eclipsing binaries can be used as distance indicators (Guinan et al. 1998), are excellent probes of stellar physics (Prša & Zwitter 2005), and offer a unique method for measuring stellar masses and other parameters as well (e.g., Andersen 1991; Torres et al. 2010).

Despite the importance of variability, the variable optical sky remains largely unexplored and poorly quantified, especially at the faint end ( $V > 15$ ). To what degree do different variable populations contribute to the overall variability, how are they distributed in magnitude and color, and what are the characteristic timescales and dominant mechanisms of variability are just some of the questions that still remain unanswered. To address these questions, several contemporary projects aimed at regular monitoring of the optical sky were started. The four most prominent wide-area (more than a few thousand  $\text{deg}^2$ ) variability surveys in terms of depth and cadence are as follows.

1. ROTSE-I (Akerlof et al. 2000) monitored the entire observable sky twice a night from  $V = 10$  to a limit of  $V = 15.5$ . The Northern Sky Variability Survey (NSVS; Woźniak et al. 2004) is based on ROTSE-I data and contains light curves for about 14 million objects, with 100–500 measurements per object collected over one year. Typical photometric precision of this data set is about 0.02 mag for sources not limited by photon statistics.

2. The All Sky Automated Survey (ASAS; Pojmański 2002) monitors the entire southern and part of the northern sky ( $\delta < +28^\circ$ ) to a limit of  $V = 14$ , including about 15 million stars. Typical photometric precision is about 0.05 mag. The third release of the ASAS Catalog of Variable Stars contains close to 50,000 variable stars. About 80% of these are new discoveries (not previously cataloged).
3. The Lowell Observatory Near Earth Objects Survey Phase I (LONEOS-I; Miceli et al. 2008) provides photometric data for  $1430 \text{ deg}^2$  of northern sky that has been imaged at least 28 times between 1998 and 2000. The LONEOS-I camera used no bandpass filter and reached a depth of  $R \sim 18.5$ . Typical photometric precision of this data set is about 0.02 mag for sources not limited by photon statistics.
4. The Palomar Transient Factory (PTF; Law et al. 2009 and Rau et al. 2009) is an ongoing wide-area, two-band (SDSS- $g'$  and Mould- $R$  filters), deep ( $R \sim 20.6$ ,  $g' \sim 21.3$ ) survey aimed at systematic exploration of the optical transient sky. As of fall 2011, PTF has observed about  $7300 \text{ deg}^2$  of northern sky at least 30 times in the Mould- $R$  band ( $\sim 1800 \text{ deg}^2$  of sky with more than 100 epochs). Typical photometric precision of this data set is better than 0.01 for sources not limited by photon statistics.

A comprehensive review of past and ongoing variability surveys can be found in Becker et al. (2004).

With hundreds of observations per object, the NSVS and ASAS data sets represent unique resources. Although a number of massive synoptic surveys, such as Pan-STARRS (Kaiser et al. 2002) and LSST (the Large Synoptic Survey Telescope; Ivezić et al. 2008), will significantly improve our knowledge of the variable faint sky, they will not obtain hundreds of observations per object any time soon.

Report Documentation Page				Form Approved OMB No. 0704-0188	
Public reporting burden for the collection of information is estimated to average 1 hour per response, including the time for reviewing instructions, searching existing data sources, gathering and maintaining the data needed, and completing and reviewing the collection of information. Send comments regarding this burden estimate or any other aspect of this collection of information, including suggestions for reducing this burden, to Washington Headquarters Services, Directorate for Information Operations and Reports, 1215 Jefferson Davis Highway, Suite 1204, Arlington VA 22202-4302. Respondents should be aware that notwithstanding any other provision of law, no person shall be subject to a penalty for failing to comply with a collection of information if it does not display a currently valid OMB control number.					
1. REPORT DATE <b>JUL 2011</b>		2. REPORT TYPE		3. DATES COVERED <b>00-00-2011 to 00-00-2011</b>	
4. TITLE AND SUBTITLE <b>Exploring the Variable Sky with Linear. I. Photometric Recalibration with the Sloan Digital Sky Survey</b>				5a. CONTRACT NUMBER	
				5b. GRANT NUMBER	
				5c. PROGRAM ELEMENT NUMBER	
6. AUTHOR(S)				5d. PROJECT NUMBER	
				5e. TASK NUMBER	
				5f. WORK UNIT NUMBER	
7. PERFORMING ORGANIZATION NAME(S) AND ADDRESS(ES) <b>California Institute of Technology, Department of Physics, Mathematics and Astronomy, 1200 East California Blvd, Pasadena, CA, 91125</b>				8. PERFORMING ORGANIZATION REPORT NUMBER	
9. SPONSORING/MONITORING AGENCY NAME(S) AND ADDRESS(ES)				10. SPONSOR/MONITOR'S ACRONYM(S)	
				11. SPONSOR/MONITOR'S REPORT NUMBER(S)	
12. DISTRIBUTION/AVAILABILITY STATEMENT <b>Approved for public release; distribution unlimited</b>					
13. SUPPLEMENTARY NOTES					
14. ABSTRACT					
15. SUBJECT TERMS					
16. SECURITY CLASSIFICATION OF:			17. LIMITATION OF ABSTRACT <b>Same as Report (SAR)</b>	18. NUMBER OF PAGES <b>13</b>	19a. NAME OF RESPONSIBLE PERSON
a. REPORT <b>unclassified</b>	b. ABSTRACT <b>unclassified</b>	c. THIS PAGE <b>unclassified</b>			

A downside of NSVS, ASAS, LONEOS, and PTF data sets is the lack of precise multi-color photometry, which can provide valuable information about sources in addition to light curve characteristics (Covey et al. 2007). The Sloan Digital Sky Survey (SDSS; York et al. 2000) has obtained five-band photometry for hundreds of millions of stars, but its temporal coverage is very poor. The only region on the sky with more than 10 observations per source is the  $\sim 300 \text{ deg}^2$  large equatorial region called Stripe 82 (Sesar et al. 2007, and references therein). At the same time, NSVS and ASAS are not deep enough to make efficient use of SDSS photometry. This goal to combine a large-area variability survey providing hundreds of observations with exquisite SDSS photometry was recently made reachable by the LINEAR survey.

The MIT Lincoln Laboratory (MITLL) has operated the Lincoln Near-Earth Asteroid Research (LINEAR) program since 1998 to search for asteroids. The focus of the program is to discover and track near-Earth asteroids (NEAs) larger than 1 km in diameter, but LINEAR has also discovered and tracked many main-belt asteroids and smaller NEAs. Since late 2002, the LINEAR program has maintained an archive of all of its imagery data. This archive now contains approximately 6 million images of the sky, most of which are 5 megapixel images covering  $2 \text{ deg}^2$ . The LINEAR image archive contains a unique combination of depth ( $V < 18$ ), coverage area, and cadence that is potentially useful in exploring a number of time-varying astronomical phenomena.

Since the LINEAR project was focused on astrometric survey, standard stars required for precise photometric calibration were often unavailable. Furthermore, a significant fraction of the data was taken in non-photometric conditions. The main purpose of this paper is to describe photometric recalibration of LINEAR data using stars observed by SDSS as photometric standards. Companion papers are discussed in Section 6.

In Section 2 we describe the LINEAR survey in more detail and discuss recalibration procedures in Section 3. The recalibrated data set is characterized in Section 4 and a preliminary analysis of about 7000 confirmed periodic variables is presented in Section 5. Our results are summarized in Section 6.

## 2. LINEAR SURVEY

### 2.1. Hardware Characteristics

The LINEAR program operates two telescopes at the Experimental Test Site located within the US Army White Sands Missile Range in central New Mexico at an altitude of 1506 m above sea level and a latitude of  $33^\circ 8' \text{N}$ . The program uses two essentially identical equatorial-mounted telescopes of the Ground-based Electro-Optical Deep Space Surveillance (GEODSS) type, usually denoted L1 and L2. Each telescope is a folded prime-focus design with a primary mirror diameter of 1.016 m and  $f/\#$  of 2.15 (Stokes et al. 2000).

The two telescopes of the LINEAR project are each equipped with a CCD camera developed at MITLL using CCDs developed and manufactured by MITLL for the US Air Force GEODSS system (Burke et al. 1998). These CCID-16 sensors are 5 megapixel ( $2560 \times 1960$ ), back-illuminated, frame-transfer CCDs with fast readout, low dark current, and low read noise. The CCID-16 sensors have eight readout regions (hereafter referred to as cells) and have high quantum efficiency over a broad part of the visible and near-infrared spectrum (with overall solar-weighted quantum efficiency of 65% and peak efficiency of 96% at 620 nm, see Figure 1). The cameras have no

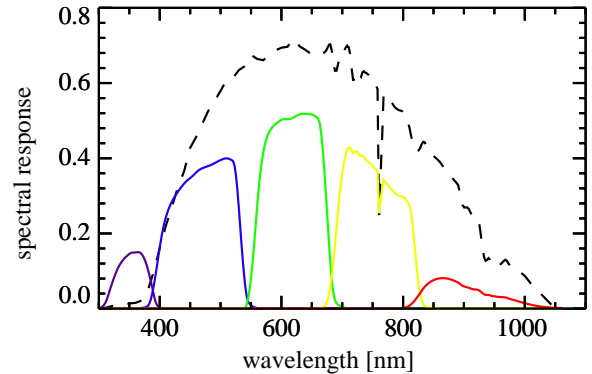


**Figure 1.** LINEAR (dashed line) and SDSS *ugriz* spectral response curves (solid lines). The response curve for LINEAR includes the spectral quantum efficiency of the back-illuminated CCD, reflectivity of the aluminum mirrors, and atmospheric transmissivity at airmass of 1.3. The response curves for SDSS include the same atmospheric absorption.

(A color version of this figure is available in the online journal.)

spectral filters. The combination of the CCID-16 camera and the 1 m GEODSS telescope produces an instantaneous field of view of  $1^\circ 60' \times 1^\circ 23'$  ( $\sim 2 \text{ deg}^2$ ), with  $2''/25$  pixels. In Section 3, the combination of CCID-16 sensors and L1 and L2 telescopes will be referred to as the L1 and L2 setups.

For a few months in 2003 (approximately August to November) the camera on the L2 telescope was replaced with a very similar camera containing a smaller format sensor called the CCID-10. This smaller sensor is identical to the CCID-16's in terms of manufacture and processing, readout electronics and settings, spectral quantum efficiency, and pixel size. The only difference between the smaller format camera and the larger format camera is the number of pixels,  $1024 \times 1024$  for the small camera, and the number of readout regions (4 cells). During the four months in 2003 that L2 was operating with the CCID-10 camera, the field of view was about  $0^\circ 64' \times 0^\circ 64'$  ( $\sim 0.4 \text{ deg}^2$ ). In Section 3, the combination of CCID-10 sensor and L2 telescope will be referred to as the small setup.

### 2.2. Observing Conditions and Cadence

The telescope site has reasonably dark skies, approaching  $\mu_V = 21 \text{ mag arcsec}^{-2}$  on the best nights. However, the LINEAR program operates on nights with suboptimal conditions including haze, bright moonlight (to within 3 days of the full moon), scattered clouds, and airglow. LINEAR images are frequently taken under skies as bright as  $\mu_V = 16 \text{ mag arcsec}^{-2}$ . The point-spread function includes unknown contributions from atmospheric seeing and various system contributions (e.g., defocus and dome airflow) and is typically around  $5''$  FWHM, resulting in slightly undersampled images.

The image integration time is allowed to vary over the seasons so that a roughly constant number of search fields fills the available dark time. During the earlier days of the LINEAR program (roughly 1998 to 2006), the integration time was 10–12 s on long winter nights and 3–5 s on short summer nights. In recent years (roughly 2007 to 2009), the integration time was increased to 15–18 s in the winter and 8–13 s in the summer. Under these observing conditions, the magnitude for which the magnitude error is  $\sim 0.2 \text{ mag}$  (the  $5\sigma$  detection limit) is about 18 mag on average.

As shown in Figure 2, the cadence of LINEAR observations (time between revisits of the same patch of sky) is fairly uniform, with a peak at  $\sim 15$  minutes and a gap at  $\sim 8 \text{ hr}$ . A more

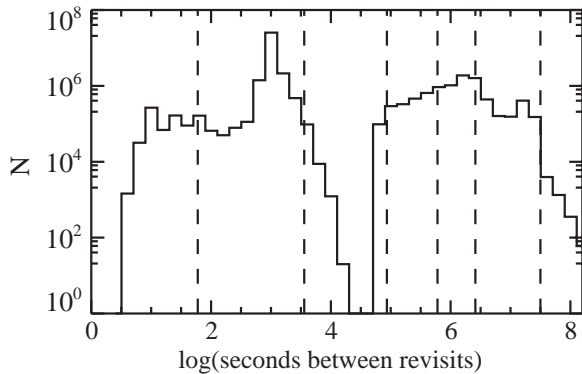


**Figure 2.** Cadence of LINEAR observations measured as the time between revisits of the same patch of sky. From left to right, the dashed lines show 1 minute, 1 hr, 1 day, 1 week, 1 month, and 1 year cadences. The LINEAR temporal coverage is fairly uniform, with a peak at  $\sim 1000$  s corresponding to the main 15 minute cadence.

detailed description of the LINEAR observing strategy is given in Appendix A.

### 2.3. Photometry and Astrometry Using SExtractor

The LINEAR project has been archiving all of its image data since 2002 December through the present. The data used for this work encompass all imagery collected from 2002 December through 2008 March. After selecting the LINEAR imagery data that overlap the main SDSS survey region (i.e., galactic latitudes greater than  $30^\circ$ ) and SDSS stripe 82 region ( $20^{\text{h}}32^{\text{m}} < \alpha_{\text{J2000.0}} < 04^{\text{h}}00^{\text{m}}$ ,  $-1^\circ26' < \delta_{\text{J2000.0}} < +1^\circ26'$ ,  $\sim 280 \text{ deg}^2$ ), the data comprise about 1.8 million images. The bias and flat-field corrections were applied to these images following standard methodology.

The extraction of sources from LINEAR images and the creation of source catalogs were done using the SExtractor software (Bertin & Arnouts 1996; see the SExtractor user’s manual<sup>6</sup> for more details on the source detection and measurement process). The preliminary astrometry for extracted sources was obtained by converting centroid pixel coordinates into equatorial J2000.0 right ascension (R.A.) and declination (decl.) by application of the gnomonic projection and a priori telescope pointing information. This projection does not correct for telescope pointing errors on the order of several pixels, telescope optical distortion on the order of a few pixels near the corners of the image, or differential refraction on the order of a few pixels at typical airmasses. When compared to the USNO-B catalog (Monet et al. 2003) astrometry, the average uncertainty in the preliminary astrometry is about  $\sim 6''$  in R.A. and decl. coordinates. Therefore, the astrometry reported by SExtractor must be recalibrated before matching extracted LINEAR sources against other catalogs. The recalibration of preliminary astrometry is described in Section 3.

The preliminary fixed-aperture photometry for each source is computed by summing the pixels within a 5 pixel ( $\sim 11''$ ) radius circular aperture and subtracting the background estimate for each pixel computed in the background estimate step. The uncertainty on the computed flux is computed assuming Poisson statistics in detected electrons with a gain conversion factor of  $2.5e^- \text{ ADU}^{-1}$ . The pixels with counts above 17,000 were not used as the CCDs begin to experience nonlinear response above

this level (corresponding to 42,000 electrons), and they saturate at full-well capacity of 75,000 electrons.

## 3. RECALIBRATION OF LINEAR ASTROMETRY AND PHOTOMETRY

In this section, we describe the astrometric and photometric recalibration of LINEAR data and quantify the quality of recalibrated data. The recalibration and data quality assessment are done on a field-by-field basis, where a field is defined as part of a LINEAR image observed by a single CCD cell (there are four cells in the small setup and eight cells in the L1 and L2 setups). The only exception to this is the astrometric recalibration, which is done on a image-by-image basis. However, the quality of astrometric recalibration is still assessed on a field-by-field basis.

### 3.1. Astrometric Recalibration

We recalibrate the preliminary astrometry using the Astrometry.net software (Lang et al. 2010). Astrometry.net uses the  $x$  and  $y$  (hereafter, pixel) positions of sources extracted by SExtractor and looks for “skymarks” (sets of four stars) that correspond to pre-computed “skymarks” found in the “clean” USNO-B catalog (Barron et al. 2008). Once a skymark is found the code obtains an initial astrometric solution (a transformation from the pixel coordinates into the J2000.0 Equatorial system) in the form of a third-degree polynomial in  $x$  and  $y$  coordinates. Using this initial astrometric solution, the code looks for additional reference USNO-B stars in the image, and further refines the initial astrometric solution when it finds them.

The quality of recalibrated LINEAR astrometry is estimated by comparing the LINEAR positions with reference USNO-B positions (Figure 3). We find that the recalibrated LINEAR single-epoch coordinates have an rms scatter of  $\sim 0''.6$  and are offset  $\lesssim 0''.3$  with respect to the USNO-B coordinates. These systematic offsets are independent of pixel positions or the position of the image on the sky and are subtracted from recalibrated LINEAR coordinates. Using a subset of data, we have found that the offsets decrease if Astrometry.net is allowed to search for even more reference USNO-B stars when refining the initial astrometric solution.

To find fields with bad astrometry, we calculate the median and rms scatter of astrometric residuals (difference between LINEAR and USNO-B positions) in R.A. and decl. for each field, and tag fields as bad if the median or rms scatter in either coordinate (R.A. or decl.) is greater than  $2''$ . We find that about 7% of all fields have bad astrometry, with the majority of bad fields ( $\sim 90\%$ ) originating from the L2 setup, and remove them from further processing. Visual inspection of images containing bad fields reveal that bad fields lack several pixel columns, which were most likely dropped due to cell readout problems.

In order to recalibrate the LINEAR photometry, we positionally matched the LINEAR data set to the SDSS Data Release 7 (SDSS DR7; Abazajian et al. 2009) imaging catalog. The SDSS DR7 imaging catalog provides homogeneous and deep ( $r < 22.5$ ) 1%–2% accurate photometry in five band-passes ( $u$ ,  $g$ ,  $r$ ,  $i$ , and  $z$ ) of more than  $11,000 \text{ deg}^2$  of the North Galactic Cap, and three stripes in the South Galactic Cap totaling  $740 \text{ deg}^2$ . The SDSS positions are accurate to better than  $0''.1$  per coordinate (rms) for sources with  $r < 20.5$  (Pier et al. 2003), and the morphological information from the images allows reliable star–galaxy separation to  $r \sim 21.5$  (Lupton et al. 2002).

<sup>6</sup> Available at <https://www.astromatic.net/pubsvn/software/sextractor/trunk/doc/sextractor.pdf>.



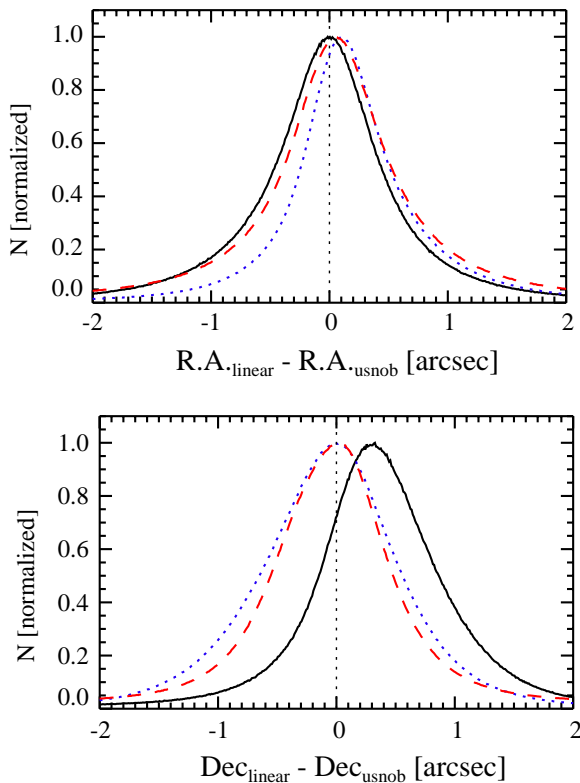


**Figure 3.** Comparison of USNO-B and recalibrated LINEAR R.A. (top) and decl. single-epoch coordinates (bottom) for the small (solid line), L1 (dotted line), and L2 (dashed line) setups. The width of the distributions (determined from the interquartile range) puts the astrometric precision in LINEAR single-epoch coordinates at  $\sim 0''.6$ . The systematic offsets in LINEAR coordinates are  $\lesssim 0''.3$  and have been subsequently corrected for. The dotted line at  $0''$  was added to guide the eye.

(A color version of this figure is available in the online journal.)

We match LINEAR sources to SDSS DR7 non-saturated, “primary” objects<sup>7</sup> using a  $3''$  radius and find  $\sim 4.8$  billion matched pairs (there are 24 million unique SDSS sources included in these pairs). There are  $\sim 1.6$  billion LINEAR sources without an SDSS match (“orphans”), and they include observations associated with stars saturated in SDSS ( $r < 13$ ,  $\sim 60\%$  of orphans), image artifacts (e.g., due to charge bleeding and diffraction spikes), moving objects such as asteroids, and other transients.

### 3.2. Photometric Recalibration

We model the recalibrated LINEAR magnitudes as

$$m_{\text{linear}} = \alpha m_{\text{instr}} + C(g - i) + Z(x, y), \quad (1)$$

where  $\alpha$  measures nonlinearity of SExtractor-supplied instrumental magnitudes  $m_{\text{instr}} = -2.5 \log(\text{counts})$ ,  $C$  is a color-dependent term that accounts for the per-exposure change in the effective central wavelength of the LINEAR bandpass, and  $Z(x, y)$  is our model for the field-specific magnitude zero-point dependent on the  $x$ - $y$  position in the image, defined as

$$Z(x, y) = Z_0 + Z_1 x + Z_2 y + F(x, y), \quad (2)$$

where  $Z_0$ ,  $Z_1$ , and  $Z_2$  vary from field to field, and  $F(x, y)$  is the “super flat field” (fixed for each observational setup). Note

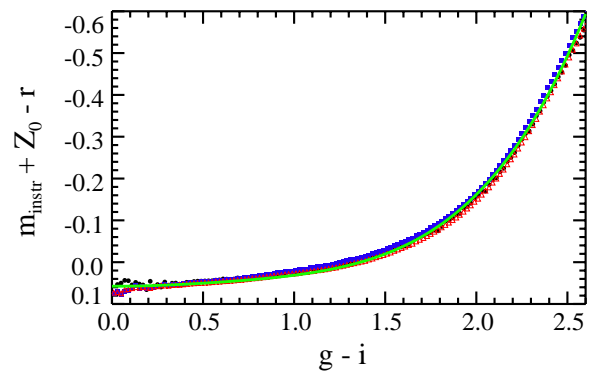


**Figure 4.** Color term between the zero-point-corrected LINEAR magnitude,  $m_{\text{instr}} + Z_0$ , and SDSS  $r$ -band magnitude for the small (dots), L1 (solid squares), and L2 (open triangles) setups. The solid line shows the best fit for all three setups. The rms scatter between the best fit for all three setups and fits to individual setups is smaller than 0.01 mag. The SDSS  $g - i$  color is not corrected for ISM extinction.

(A color version of this figure is available in the online journal.)

that the color-independent airmass term (gray extinction) is implicitly included in  $Z_0$ .

To recalibrate the LINEAR photometry, we need a catalog of photometric standard stars in the LINEAR photometric (unfiltered) system. Since such a catalog does not exist, we use the SDSS imaging catalog and utilize SDSS  $gri$  photometry to derive magnitudes in the LINEAR photometric system.

#### 3.2.1. LINEAR Magnitudes Synthesized from SDSS Photometry

We define LINEAR magnitudes synthesized from the SDSS photometry as

$$m_{\text{sdss}} = r + f(g - i), \quad (3)$$

where  $f(g - i)$  is some function of  $g - i$  and SDSS  $gri$  magnitudes are *not* corrected for the ISM extinction.

We find  $f(g - i)$  iteratively by first adopting  $\alpha = 1.0$  in Equation (1),  $F(x, y) = 0$  in Equation (2), and  $f(g - i) = 0$  in Equation (3). For each field, we determine  $Z_0$ ,  $Z_1$ , and  $Z_2$  by minimizing

$$\chi^2 = \Sigma[(m_{\text{linear}} - m_{\text{sdss}})/\sigma_{\text{linear}}]^2, \quad (4)$$

where  $\sigma_{\text{linear}}$  is the magnitude error supplied by the SExtractor (errors in  $m_{\text{sdss}}$  are assumed to be much smaller than errors in  $m_{\text{linear}}$ ).

The LINEAR observations of calibration stars must be matched within  $2''$  to isolated,<sup>8</sup> unresolved, SDSS objects brighter than  $r = 17$ , with  $0 < g - i < 2.6$ . Having  $Z(x, y)$  for each field, we calculate  $m_{\text{instr}} + Z(x, y) - r$  residuals for all calibration stars, bin the values in  $g - i$  bins, and plot the median residuals in Figure 4 for the small, L1, and L2 setups. We plot medians for each setup separately because each setup represents a separate optical, and therefore photometric, system.

Even though the three setups are different, their residuals depend similarly on  $g - i$  (rms scatter around the mean is 0.01 mag), as indicated by medians plotted in Figure 4. We therefore fit a fourth-degree polynomial to all medians and obtain

$$f(g - i) = 0.0574 + 0.004(g - i) - 0.056(g - i)^2 + 0.052(g - i)^3 - 0.0262(g - i)^4. \quad (5)$$

<sup>7</sup> See <http://cas.sdss.org/dr6/en/help/docs/algorithm.asp?key=flags>.

<sup>8</sup> SDSS CHILD flag set to 0.

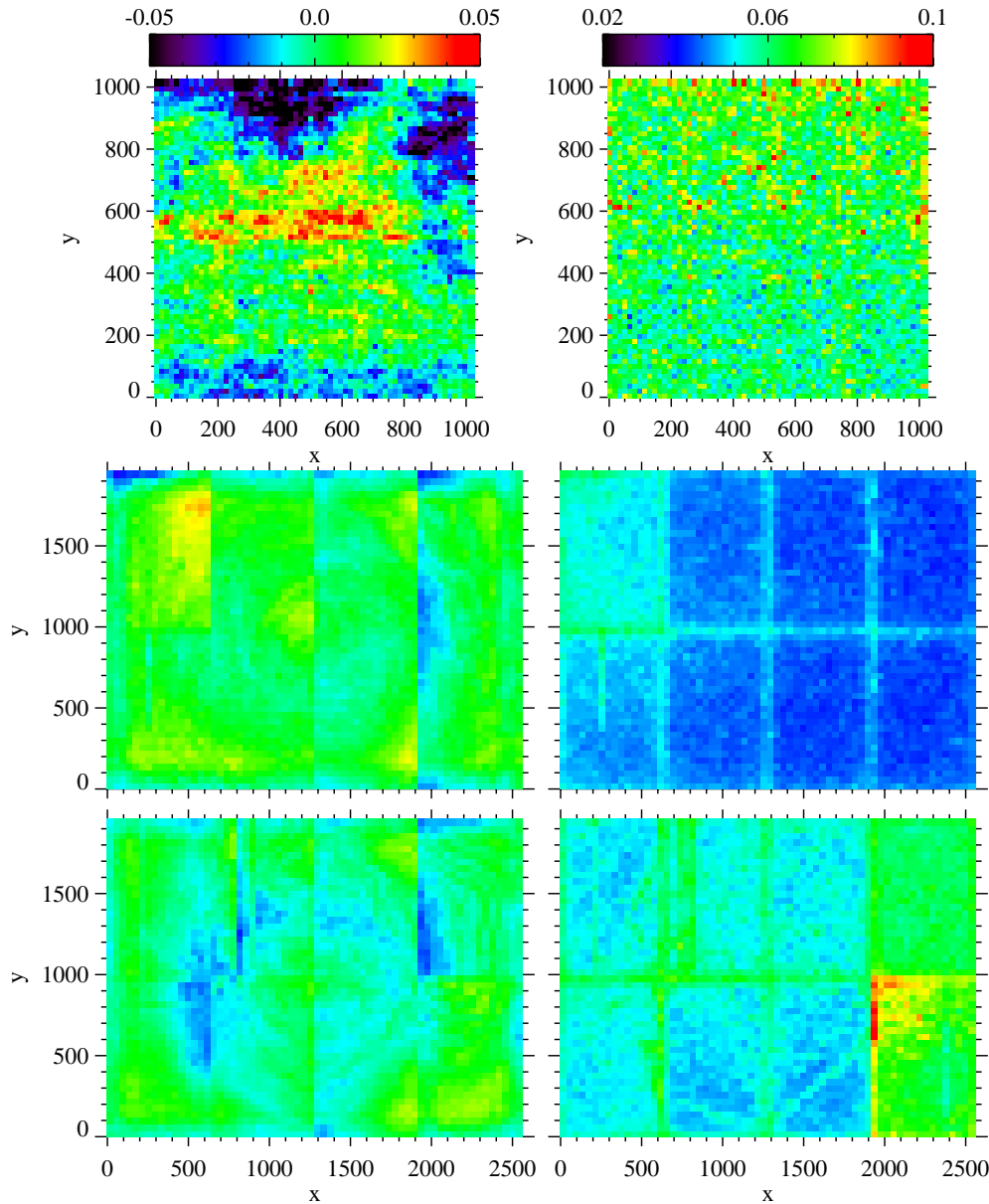


**Figure 5.** Distribution of  $m_{\text{linear}} - m_{\text{sdss}}$  residuals binned in the  $x$ - $y$  plane for the small (top), L1 (middle), and L2 (bottom) setups. The panels on the left show median values in each bin, and the panels on the right show rms scatter in a bin. The values are color-coded according to legends, with values outside the range saturating. The patterns seen on the left are magnitude zero-point variations that were not taken out when LINEAR images were flat fielded. Therefore, the maps on the left represent “super flat fields” that need to be subtracted during recalibration.

(A color version of this figure is available in the online journal.)

The transformation from SDSS  $gri$  to LINEAR magnitudes, as defined by Equation (3), is then

$$m_{\text{sdss}} = r + 0.0574 + 0.004(g - i) - 0.056(g - i)^2 + 0.052(g - i)^3 - 0.0262(g - i)^4. \quad (6)$$

This equation effectively turns the SDSS imaging catalog into a catalog of LINEAR photometric standard stars.

### 3.2.2. Super Flat Fields and Nonlinearity of Instrumental Magnitudes

We find the super flat field,  $F(x, y)$ , iteratively by first adopting  $\alpha = 1.0$  in Equation (1) and  $F(x, y) = 0$  in Equation (2). For each field, we determine  $Z_0$ ,  $Z_1$ ,  $Z_2$ , and  $C$  by minimizing Equation (4) using calibration stars brighter than  $m_{\text{sdss}} = 17$ . The super flat-field correction,  $F(x, y)$ , is then obtained by finding

the median of  $m_{\text{linear}} - m_{\text{sdss}}$  residuals binned in  $x$ - $y$  pixels, and is shown as a color-coded map in Figure 5 (left) for each observational setup. Figure 6 (left) shows the residuals after the subtraction of Figure 5 (left) maps. On average, the median residuals are now smaller than 0.005 mag, compared to  $\sim 0.02$ – $0.03$  mag before the correction was made.

To verify our assumption of  $\alpha = 1.0$  (the linearity of instrumental magnitudes), we adopt  $\alpha = 1.0$  in Equation (1), and determine  $Z_0$ ,  $Z_1$ ,  $Z_2$ , and  $C$  by minimizing Equation (4) using calibration stars brighter than  $m_{\text{sdss}} = 17$ . We bin  $m_{\text{linear}} - m_{\text{sdss}}$  residuals in  $m_{\text{sdss}}$  bins, and plot the medians as a function of  $m_{\text{sdss}}$  in Figure 7. A strong dependence of residuals on  $m_{\text{sdss}}$  would indicate nonlinear ( $\alpha \neq 1.0$ ) behavior of instrumental magnitudes. With the exception of a small nonlinearity ( $< 0.02$  mag) in the L1 setup for  $m_{\text{sdss}} < 15$ ,

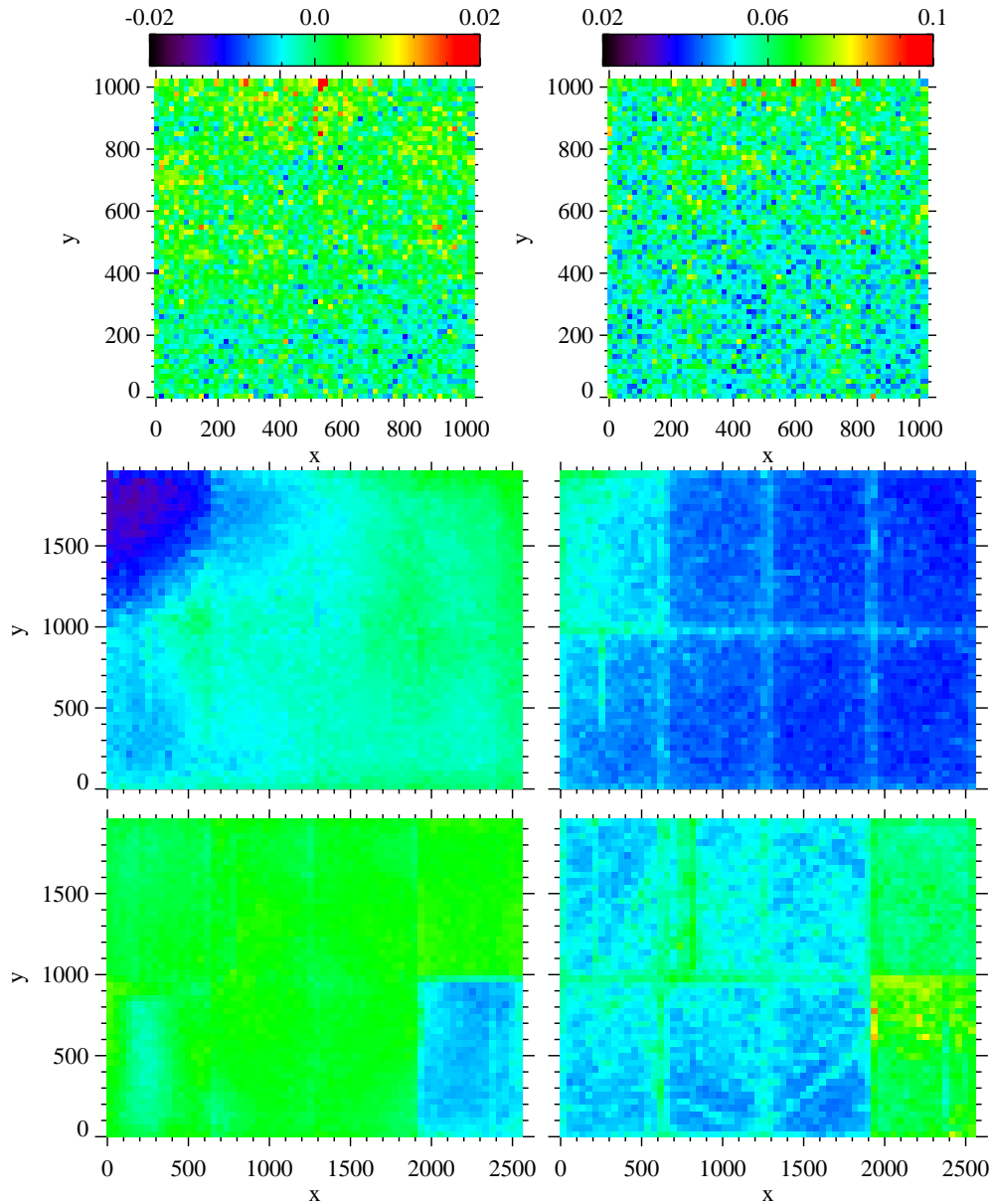


**Figure 6.** Similar to Figure 5, but obtained after subtraction of “super flat fields.” The median values are color coded on a smaller range than in Figure 5 (0.02 mag vs. 0.05 mag). On average, the medians are now smaller than 0.005 mag, and the rms scatter is smaller than 0.05 mag. The higher rms scatter indicates cells with sometimes problematic readouts.

(A color version of this figure is available in the online journal.)

the residuals do not depend on magnitude, indicating that the  $\alpha = 1.0$  assumption is valid.

To estimate the magnitude of correction introduced by including the color-dependent term  $C$  (accounts for the change in LINEAR bandpass due to varying airmass) in Equation (1), we measure the rms scatter of  $C(g-i)$  values obtained from all calibration stars and fields. We find the rms scatter to be  $\sim 0.02$  mag, indicating that by correcting for this term the systematic uncertainty in LINEAR photometry is reduced by  $\sim 0.02$  mag. On the other hand, the inclusion of the  $Z_0$  term is much more important as it reduces the systematic uncertainty in LINEAR photometry by  $\sim 0.3$  mag (the rms scatter of  $Z_0$  values is  $\sim 0.3$  mag).

Once the color-dependent term,  $C$ , and the zero point,  $Z(x,y)$ , are obtained for a field, the LINEAR photometry for that field is recalibrated using Equation (1). For “orphan” sources (LINEAR

sources not associated with SDSS objects) the color-dependent term is set to  $C = 0$ , as  $g-i$  colors are not available for these sources. Therefore, the systematic uncertainty in recalibrated photometry is slightly higher for orphans (by  $\sim 0.02$  mag).

### 3.2.3. Checks on Recalibrated Photometry

To quantify the quality of recalibration on a field-to-field basis, we calculate  $m_{\text{linear}} - m_{\text{sdss}}$  residuals for calibration stars, and find their median and rms scatter (determined from the interquartile range) for each field. The median of  $(m_{\text{linear}} - m_{\text{sdss}})$  residuals per field is then an estimate of the zero-point error. The distribution of these median offsets, shown in Figure 8, is about 0.01 mag wide and demonstrates the overall quality of recalibrated photometry. About 10% of fields are of low quality (rms scatter in  $m_{\text{linear}} - m_{\text{sdss}} > 0.1$  mag), usually due to highly

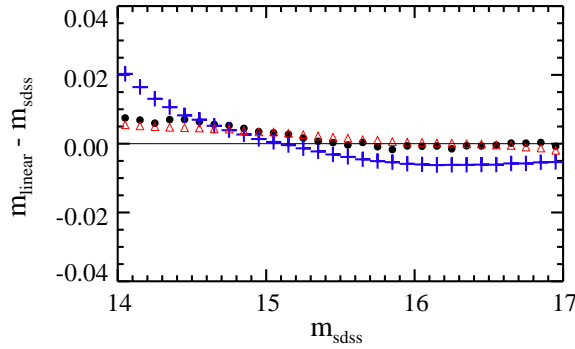


**Figure 7.** Medians of  $m_{\text{linear}} - m_{\text{sdss}}$  residuals in  $m_{\text{sdss}}$  bins for the small (dots), L1 (crosses), and L2 setups (open triangles). Apart from slight non-linearity ( $<0.02$  mag) in the L1 setup at bright magnitudes, recalibrated LINEAR magnitudes are linear with magnitudes synthesized from SDSS *gri* photometry. (A color version of this figure is available in the online journal.)

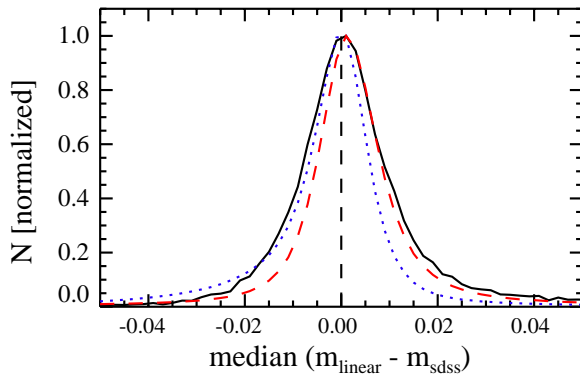


**Figure 8.** Distribution of zero-point offsets between SDSS and LINEAR systems for the small (solid line), L1 (dotted line), and L2 (dashed line) setups, where the offset is measured for each field as the median of  $m_{\text{linear}} - m_{\text{sdss}}$  residuals. The distribution is about 0.01 mag wide, implying that on average the LINEAR recalibration is about 0.01 mag offset from the SDSS photometric system. (A color version of this figure is available in the online journal.)

variable cloud coverage. Sources detected in such fields are removed from further consideration.

Another useful statistic is the rms scatter of  $\chi$  values,  $(m_{\text{linear}} - m_{\text{sdss}})/\sigma_{\text{linear}}$ , in  $m_{\text{sdss}}$  bins. This rms scatter should be equal to 1 and should not depend on  $m_{\text{sdss}}$  if the SExtractor-supplied magnitude errors ( $\sigma_{\text{linear}}$ ) are correct Gaussian errors. As shown in Figure 9, the rms scatter is greater than 1 indicating underestimated  $\sigma_{\text{linear}}$  errors by up to a factor of  $\sim 2$ .

We correct the underestimated magnitude errors by multiplying them by 1.4, 1.85, and 1.65 for the small, L1, and L2 setups, respectively. In the case of the small setup, the factor of 1.4 is only the average value as SExtractor-supplied magnitude errors for that setup seem to depend on magnitude. Therefore, the magnitude errors for the small setup may be slightly overestimated or underestimated depending on the brightness of the source. This is not a major issue as only a small fraction of all LINEAR sources ( $\sim 0.1\%$ ) originate from the small setup.

The reason for this underestimation of SExtractor-supplied magnitude errors is not clear. Non-inclusion of systematic errors (e.g., due to flat fielding) in  $\sigma_{\text{linear}}$  cannot explain this behavior for L1 and L2 setups. If additive systematic errors were the reason for this underestimation, then  $(m_{\text{linear}} - m_{\text{sdss}})/\sigma_{\text{linear}}$  should decrease with magnitude because  $\sigma_{\text{linear}}$  is expected to increase with magnitude (see Figure 13). Yet, no such decrease is seen in Figure 9 for L1 and L2 setups.

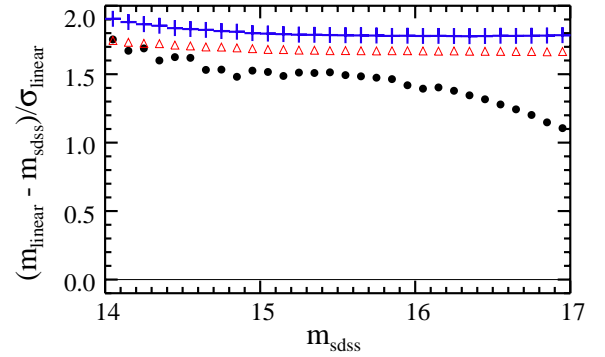


**Figure 9.** rms scatter of  $(m_{\text{linear}} - m_{\text{sdss}})/\sigma_{\text{linear}}$  values in  $m_{\text{sdss}}$  bins for the small (dots), L1 (crosses), and L2 (open triangles) setups. The rms scatter values greater than 1 indicate underestimated LINEAR magnitude errors. The pipeline-supplied errors for the small, L1, and L2 setups are underestimated by about 40%, 85%, and 65%, respectively. (A color version of this figure is available in the online journal.)

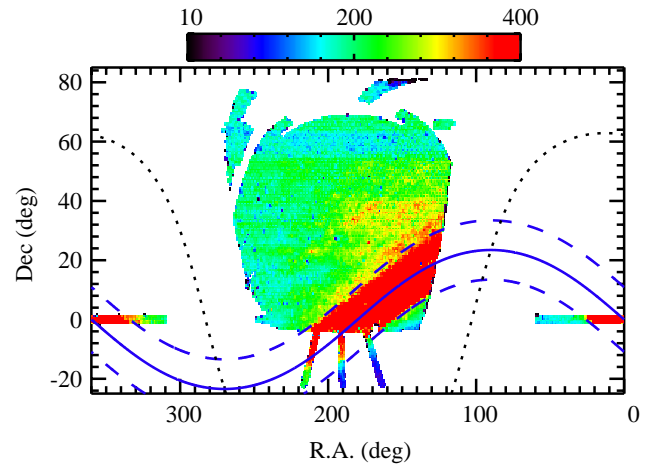


**Figure 10.** Median number of observations per object as a function of equatorial J2000.0 right ascension and declination coordinates. The values are color-coded according to the legend, with values outside the range saturating. The dashed lines show  $\pm 10^\circ$  of the ecliptic plane (solid line) and the Galactic plane is shown as a dotted line. The average number of observations per object within  $\pm 10^\circ$  of the ecliptic plane is  $\sim 460$ , and  $\sim 200$  elsewhere. (A color version of this figure is available in the online journal.)

#### 4. CHARACTERIZATION OF THE RECALIBRATED LINEAR DATA SET

There are about 5 billion sources in the recalibrated LINEAR data set. These sources were grouped into clusters using an implementation of the OPTICS algorithm (Ankerst et al. 1999) and a clustering radius of  $2''$ . There are about 25 million clusters with more than 15 observations. SDSS provides morphological classification for 24 million clusters (7 million are resolved and 17 million are unresolved by SDSS), and for 1 million of these clusters there is no SDSS classification (they are slightly outside the SDSS footprint). Clusters with 15 or more sources are hereafter labeled as LINEAR objects or time series. The median number of epochs (observations) per object as a function position and magnitude is shown in Figures 10 and 11. The average number of epochs for objects brighter than 18 mag within  $\pm 10^\circ$  of the ecliptic plane is  $\sim 460$ , and  $\sim 200$  elsewhere.

Clusters with less than 15 sources are not tagged as objects. We have statistically analyzed properties of 385 million sources ( $\sim 8\%$  of all LINEAR sources) assigned to such clusters and



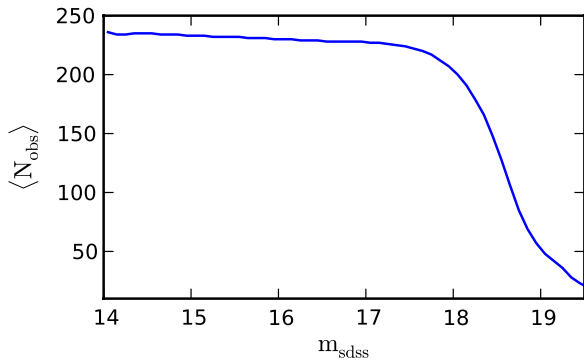


**Figure 11.** Median number of “good” observations (observations with flags = 0) as a function of  $m_{\text{sdss}}$ . The median number of “good” observations is  $\sim 200$  for  $m_{\text{sdss}} < 18$ , after which it decreases precipitously (the  $5\sigma$  detection limit is at  $m_{\text{sdss}} \sim 18$ ). About 10% of detections have flags  $> 0$ .

(A color version of this figure is available in the online journal.)

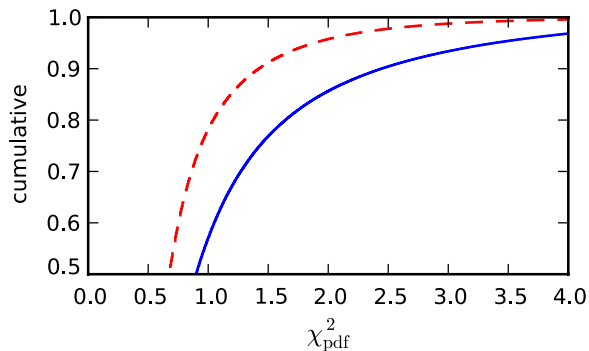


**Figure 12.** Cumulative distribution of  $\chi^2_{\text{pdf}}$  values for a bright ( $14.5 < \langle m_{\text{linear}} \rangle < 17$ , solid line) and faint ( $17 < \langle m_{\text{linear}} \rangle < 18$ , dashed line) sample of LINEAR objects. The median of distributions is  $\sim 1$ , indicating that, on average, the uncertainties in LINEAR magnitudes are well determined. The high-end tail of distributions ( $\chi^2_{\text{pdf}} > 3$ ) is populated by truly and spuriously variable objects (most likely dominated by the latter).

(A color version of this figure is available in the online journal.)

have found that most of them are very faint ( $m_{\text{linear}} > 19.5$ ), have very uncertain magnitudes ( $\sigma_{\text{linear}} > 0.4$  mag), and have high ellipticity (suggestive of cosmic rays and image artifacts). Such clusters and their observations are not included in our database. This also means that the LINEAR database does not include observations of fast moving objects (i.e., objects moving faster than  $\sim 1'' \text{ day}^{-1}$ ).

In order to enable the discovery of variable objects and to further characterize the LINEAR data set, we have computed various low-order statistics for time series, such as the median recalibrated magnitude ( $\langle m_{\text{linear}} \rangle$ ), rms scatter ( $\sigma$ ),  $\chi^2$  per degree of freedom ( $\chi^2_{\text{pdf}}$ ), skewness ( $\gamma_1$ ), and kurtosis ( $\gamma_2$ ). The cumulative distributions of  $\chi^2_{\text{pdf}}$  for LINEAR objects with more than 30 observations are shown in Figure 12.

The median of the  $\chi^2_{\text{pdf}}$  distribution for bright LINEAR objects ( $14.5 < \langle m_{\text{linear}} \rangle < 17$ ) is about 1, indicating that, on average, the uncertainties in LINEAR magnitudes are well determined. For fainter LINEAR objects ( $17 < \langle m_{\text{linear}} \rangle < 18$ ), the median of the  $\chi^2_{\text{pdf}}$  distribution is slightly lower ( $\sim 0.7$ ) indicating slightly overestimated photometric errors.

The high-end tail ( $\chi^2_{\text{pdf}} > 3$ ) of the cumulative  $\chi^2_{\text{pdf}}$  distribution suggests that  $\sim 5\%$  of bright LINEAR objects exhibit deviations from the mean that are inconsistent with the Gaussian distribution of errors. These objects could be variable

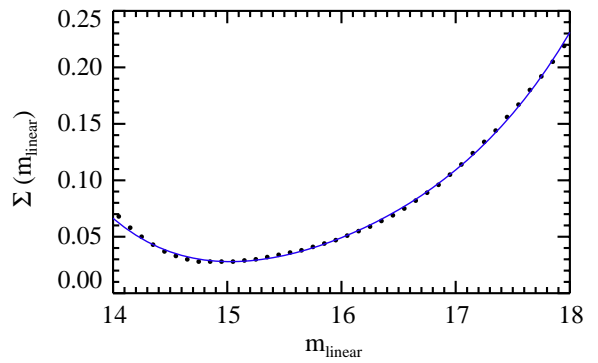


**Figure 13.** Median photometric error,  $\Sigma$ , as a function of magnitude. The median photometric error is estimated as the median of  $\sigma$  values in a magnitude bin (dots), where  $\sigma$  is the rms scatter of a time series. The analytic description of  $\Sigma(m_{\text{linear}})$  is given by Equation (7) (solid line), and was obtained by fitting a fourth-degree polynomial to medians. The median photometric error increases rapidly from about 0.03 mag at 15 mag, where systematic errors dominate, to 0.2 mag at 18 mag, where the errors are dominated by photon statistics.

(A color version of this figure is available in the online journal.)

or could have unreliable (non-Gaussian) errors. While it is not impossible that some fraction of LINEAR objects are variable ( $\sim 1\%$  of sources brighter than  $r = 20$  are variable; see Sesar et al. 2006, and references therein), a fraction of  $\sim 5\%$  seems unlikely. A more likely explanation is spurious variability induced by non-Gaussian errors, caused by blending of sources and unaccounted instrumental defects (e.g., bad pixels).

To estimate the dependence of the median photometric error ( $\Sigma$ ) on magnitude, we follow Sesar et al. (2007) and calculate median  $\sigma$  values in  $\langle m_{\text{linear}} \rangle$  bins. The dependence of median  $\sigma$  on  $\langle m_{\text{linear}} \rangle$ , as shown in Figure 13, can be modeled as a fourth-degree polynomial:

$$\Sigma(x) = 122.995 - 30.346x + 2.8183x^2 - 0.116893x^3 + 0.0018295x^4, \quad (7)$$

where  $x = m_{\text{linear}}$ . The smallest photometric errors are at  $m_{\text{linear}} \sim 15$  ( $\sim 0.03$  mag) and are limited by systematic errors in calibration. The increase in photometric error at brighter magnitudes is probably due to saturation issues in LINEAR. The photometric error starts to increase rapidly toward fainter magnitudes due to photon noise and reaches  $\sim 0.2$  mag at  $m_{\text{linear}} \sim 18$  (the adopted faint limit).

In addition to statistics calculated on light curves, we also calculated time-averaged positions (median and mean R.A. and decl.). To estimate the reliability of time-averaged LINEAR positions, we compared them to SDSS positions in  $\sim 1 \text{ deg}^2$  pixels on the sky and calculated the median difference in positions for each pixel. We find that, on average, the time-averaged LINEAR positions are within  $0''.3$  of SDSS positions, with no systematic trends across the sky. The largest median difference (for a  $\sim 1 \text{ deg}^2$  pixel) is  $\sim 1''.5$ . While this precision is sufficient for most applications, we still recommend that SDSS positions are used whenever possible to avoid patches where time-averaged LINEAR positions may be less reliable.

Since SDSS is about 4 mag deeper than LINEAR, it can be used to estimate the completeness of the LINEAR object catalog (i.e., LINEAR object catalog is a subset of the SDSS object catalog). To estimate the completeness of the LINEAR object catalog, in Figure 14 we plot the fraction of SDSS objects matched to LINEAR objects as a function of  $m_{\text{sdss}}$  (LINEAR magnitude synthesized from SDSS photometry; see

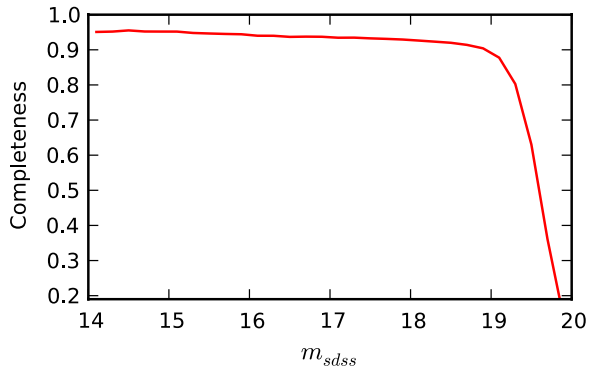


**Figure 14.** Completeness of the LINEAR catalog as a function of  $m_{\text{sdss}}$  magnitude (LINEAR magnitude synthesized from SDSS photometry, see Equation (6)). The completeness is estimated as a fraction of SDSS objects matched to LINEAR objects within  $2''$ . We find the object catalog to be more than 90% complete for  $m_{\text{sdss}} < 19$ .

(A color version of this figure is available in the online journal.)

Equation (6)). For this purpose, we use SDSS and LINEAR objects with  $0 < g - i < 2.5$  (color range where Equation (6) is valid),  $170^\circ < \text{R.A.} < 220^\circ$ , and  $15^\circ < \text{decl.} < 65^\circ$ . As shown in Figure 14, the LINEAR *object* catalog is more than 90% complete for  $m_{\text{sdss}} < 19$ . This estimate may be a bit misleading as the criterion for object creation is having at least 15 detections. Even faint objects ( $18 < m_{\text{sdss}} < 19.5$ ) are likely to be detected at least 15 times out of an average of 200 observations (see Figure 11), if the observing conditions are better than average (e.g. due to better seeing and darker skies).

## 5. PRELIMINARY ANALYSIS OF VARIABLE OBJECTS SELECTED FROM THE LINEAR DATA SET

We have examined a small subset of objects with  $\chi_{\text{pdf}}^2 > 3$  ( $\sim 5000$ ) and identified a subset of periodically variable stars. We confirmed expectation from the preceding section that only a few percent of the  $\chi_{\text{pdf}}^2 > 3$  subsample are convincing cases of periodic variability. As an illustration of the quality of LINEAR light curves at the bright ( $\langle m_{\text{linear}} \rangle \sim 15$ ) and faint ( $\langle m_{\text{linear}} \rangle \sim 17$ ) ends, we show their period-folded light curves in Figure 15. The main strength of the LINEAR survey is easily discernible in these plots: even at the faint end, the light curve features are well defined, thanks to dense LINEAR sampling.

To exploit the full potential of the LINEAR photometric database, an automated selection and classification of variable objects is desirable. This desideratum is not easy to accomplish because the fraction of spurious objects with  $\chi_{\text{pdf}}^2 > 3$  is an order of magnitude larger than the fraction of truly variable objects. In order to enable the deployment of automated selection and classification methods, we have undertaken an extensive program of visual light curve classification. Details of this program are described in a companion paper (L. Palaversa et al. 2011, in preparation, hereafter Paper II) and here we only provide a brief description of the variable candidate selection and their distribution in various color-color diagrams.

In the first step, we define a flux-limited sample of objects with  $14.5 < \langle m_{\text{linear}} \rangle < 17$  and select about 200,000 light curves with  $\chi_{\text{pdf}}^2 > 3$  and  $\sigma > 0.1$  mag ( $\sigma$  is the rms scatter in the light curve). We limit classification to objects exhibiting periodic variability and use phased light curves for visual inspection.

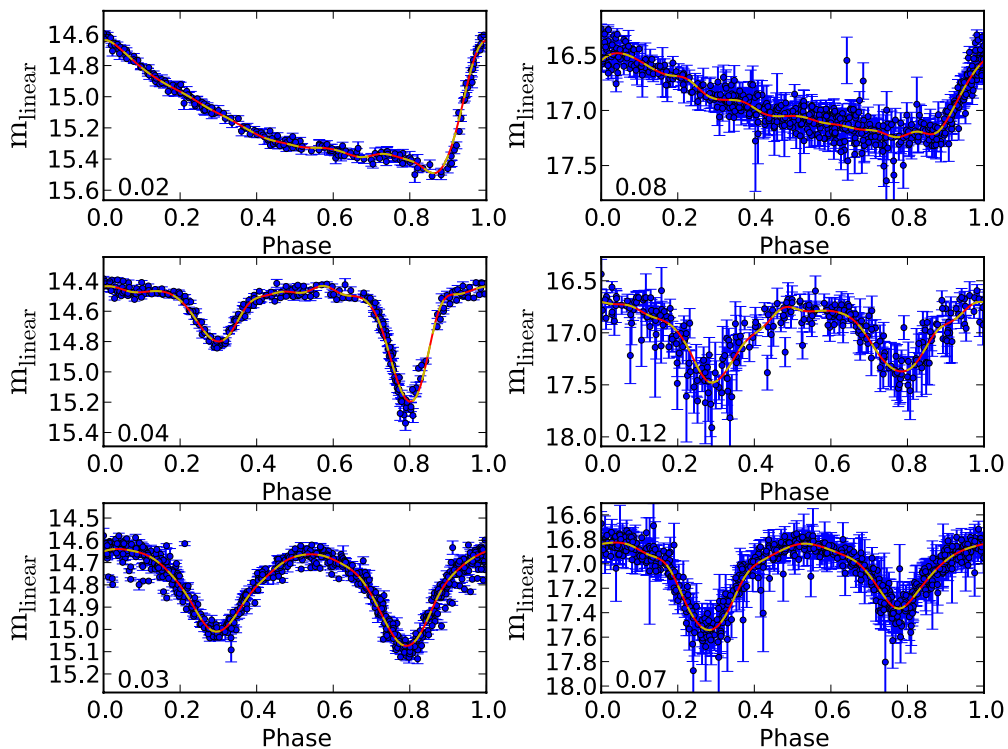


**Figure 15.** Examples of period-folded light curves from the LINEAR data set. The left panels show bright ( $\langle m_{\text{linear}} \rangle \sim 15$ ) and right panels show faint objects ( $\langle m_{\text{linear}} \rangle \sim 17$ ). The two top light curves are RR Lyrae stars, and other are eclipsing binary systems. The number in the lower left corner in each panel indicates the rms scatter around the cubic spline fit to the binned mean values of the light curve using 20 points (dashed line). The light curve features are well defined, thanks to dense LINEAR sampling, even for faint stars.

(A color version of this figure is available in the online journal.)

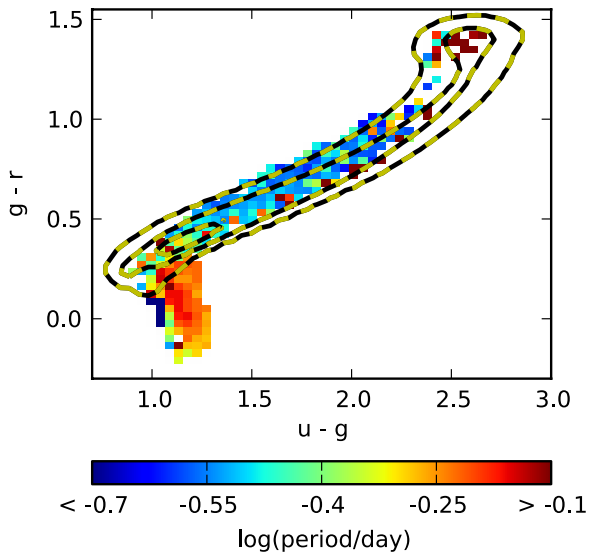


**Figure 16.** Distribution of  $\log(\text{period})$  for  $\sim 7000$  LINEAR variables in the SDSS  $u-g$  vs.  $g-r$  color-color diagram. The sample is limited to  $14.5 < r < 17$  and variability was confirmed by visual classification of light curves. Sources are binned in 0.05 mag wide color bins, and the median values are color-coded according to the legend on the right (values outside the range saturate in blue or red). Contours outline the overall distribution of SDSS stars (with  $14.5 < r < 17$ ) at 1%, 10%, and 50% of the peak density.

(A color version of this figure is available in the online journal.)

The periods are determined using the Supersmoother algorithm (Reimann 1994). In total, about 7000 LINEAR objects (3.5% out of 200,000) were visually confirmed as periodic variables, with about two-thirds classified as RR Lyrae type *ab* stars and eclipsing binary stars of all types. The remaining 1/3 include SX Phoenicis and Delta Scuti stars, long-period variables, as well as possible RR Lyrae type *ab* and eclipsing binary stars with less certain classification. The distributions of classified objects in the SDSS  $u-g$  versus  $g-r$  color-color diagram is shown in Figure 16.

The differences between the distributions of all sources and those of the confirmed variable subsample demonstrate that the latter are robustly classified (i.e., the classification is not random). The most obvious difference is a much higher fraction of RR Lyrae stars in the classified sample ( $u-g \sim 1.15$ ,  $g-r < 0.3$ ). The eclipsing binary systems of all types dominate the visually classified sample in the main stellar locus region. There seems to be a hint for the median period of eclipsing binaries becoming longer for bluer stars. The distribution of eclipsing stars is offset from the distribution of all stars in the direction perpendicular to the stellar locus (offset to upper left). There is also a lack of variable (eclipsing) systems of the late-K and early-M spectral type. These results are discussed in more detail in Paper II.

## 6. SUMMARY

In this work, we have described astrometric and photometric recalibration of data obtained by the asteroid survey LINEAR. The public access to the recalibrated LINEAR data set will be provided through the SkyDOT Web site (<http://skydot.lanl.gov>). A description of various cataloged parameters that are available in this database is given in Appendix B.

The preliminary astrometry produced by the survey has been recalibrated using the Astrometry.net software and USNO-B

catalog as the reference astrometric catalog. The precision (rms scatter) of single-epoch-recalibrated LINEAR coordinates is  $\sim 0''.6$  with respect to the reference (USNO-B) astrometric catalog. The precision of time-averaged LINEAR coordinates is  $\sim 0''.3$  with respect to SDSS positions.

In order to recalibrate the LINEAR photometry, we positionally matched the LINEAR data set to the SDSS DR7 imaging catalog and used SDSS as a catalog of photometric standard stars. LINEAR instrumental magnitudes were corrected for changes in the LINEAR bandpass (due to varying airmass) and for zero-point variations across the CCD (due to imperfect flat fielding). These corrected LINEAR magnitudes were then offset on a per-LINEAR field basis to match the SDSS magnitude zero-point system. In general, the recalibrated LINEAR magnitudes ( $m_{\text{linear}}$ ) behave linearly, with the exception of a small nonlinearity ( $< 0.02$  mag) in the L1 setup at magnitudes brighter than 15 mag.

We find the average uncertainty in recalibrated LINEAR magnitudes to be  $\sim 0.03$  mag at the bright end ( $m_{\text{linear}} \sim 15$ , the systematic uncertainty) and  $\sim 0.2$  mag at the faint end ( $m_{\text{linear}} \sim 18$ , the adopted faint limit for the survey). The SExtractor-supplied magnitude errors were found to be underestimated by 40%–85%, independent of magnitude, and were subsequently corrected for this behavior using multiplicative factors.

There are about 5 billion photometric measurements in the recalibrated LINEAR data set. The sources detected in each observation were grouped into clusters (time series or objects) using a clustering radius of  $2''$ . There are about 25 million clusters with at least 15 observations (7 million resolved and 17 million unresolved by SDSS, the rest without morphological classification). The median number of epochs (observations) per object brighter than 18 mag and within  $\pm 10^\circ$  of the ecliptic plane is  $\sim 460$ , and  $\sim 200$  elsewhere. The completeness of the LINEAR object catalog (relative to the SDSS imaging catalog) was estimated to be better than 90% for sources brighter than 19 mag.

LINEAR data set represents a major new resource for studying the variability of faint optical sources. With an average of 200 observations per object, LINEAR data provide time domain information for the brightest four magnitudes of the SDSS survey. At the same time, LINEAR significantly extends the deepest similar wide-area variability survey, the Northern Sky Variability Survey, by 3 mag.

In order to help automated discovery of variable objects, we have computed various low-order statistics for time series (median recalibrated magnitude, rms scatter,  $\chi^2$  per degree of freedom, skewness, and kurtosis). The  $\chi^2_{\text{pdf}}$  distribution for bright LINEAR objects (brighter than 17 mag) is centered at  $\sim 1$  (indicating that, on average, the uncertainties in LINEAR magnitudes are well determined), and has a long high-end ( $\chi^2_{\text{pdf}} > 3$ ) tail. About 5% of LINEAR objects have  $\chi^2_{\text{pdf}} > 3$ ; in a sample with Gaussian errors, less than 0.01% of objects are expected to have  $\chi^2_{\text{pdf}} > 3$ . This high-end tail is populated by truly variable objects, but is most likely dominated by spuriously variable objects with unreliable (non-Gaussian) errors (caused by, for example, unaccounted instrumental defects such as bad pixels or by blended sources).

Since the fraction of spurious variable objects is at least a few times greater than the fraction of truly variable objects, we have undertaken an extensive program of visual light curve classification in order to enable future deployment of automated methods. Details of this program are described in a companion paper (L. Palaversa et al. 2011, in preparation).

B. Sesar thanks NSF grant AST-0908139 to J. G. Cohen and NSF grant AST-1009987 to S. R. Kulkarni for partial support. Ž.I. acknowledges support by NSF grants AST-0707901 and AST-1008784 to the University of Washington, by NSF grant AST-0551161 to LSST for design and development activity, and by the Croatian National Science Foundation grant O-1548-2009. Partial support for this work was provided by NASA through a contract issued by the Jet Propulsion Laboratory, California Institute of Technology under a contract with NASA. The LINEAR program is sponsored by the National Aeronautics and Space Administration (NRA Nos. NNH09ZDA001N, 09-NEOO09-0010) and the United States Air Force under Air Force Contract FA8721-05-C-0002. Opinions, interpretations, conclusions, and recommendations are those of the authors and are not necessarily endorsed by the United States Government. This research made use of tools provided by Astrometry.net.

## APPENDIX A

### LINEAR OBSERVING STRATEGY

To search for asteroids, the LINEAR program attempts to cover the entire portion of sky available from the site each lunar month (lunation), with repeat searches within  $10^\circ$  to  $15^\circ$  of the ecliptic plane. The program schedules searches on both telescopes an average of 25 nights per lunation, taking off 4–5 nights around the full moon. After accounting for weather and equipment problems, about 20 observing nights are achieved per lunation with each telescope. To minimize stray light, the survey fields are kept about  $20^\circ$  away from the moon during the week before and after the full moon.

To efficiently cover the available sky at minimal airmass, each telescope is assigned a strip of sky that is aligned with either the ecliptic or the equator and is typically 3–4 fields of view ( $4^\circ$ – $5^\circ$ ) wide in declination or ecliptic latitude, and 150 fields of view ( $240^\circ$ ) long in right ascension or ecliptic longitude. The search box is divided into 5–7 regions, each containing about 100 fields. The regions are searched starting with the westernmost region at the beginning of astronomical twilight in the evening, and ending with the easternmost region at the end of astronomical twilight in the morning. All of the fields in a single region are imaged in sequence, and then the sequence is repeated in that

region four more times. The five images of a given field are combined into a “frameset” which forms the input to a moving target detection algorithm that distinguishes asteroids from stars and noise based on their motion. This process of cycling through the fields in a region five times produces a temporal separation of 15–20 minutes between successive images of the same patch of sky.

On subsequent nights, the entire search area for each telescope is generally stepped north or south by the height of the region in order to cover the entire sky, though gaps are occasionally unavoidable due to missed nights. Over the course of one lunation the entire available sky is generally searched once, and areas within about  $10^\circ$  of the ecliptic are searched two or three times. Because the monthly search regions are quite wide in right ascension, there is significant overlap in coverage area on adjacent lunar months. Therefore, a given patch of sky can be observed up to eight months in a row before it passes into the daytime portion of the sky for four months. After a full year the search covers the entire sky north of declination  $-30^\circ$  except for a small circle north of declination  $82^\circ$  where the telescope has poor settling ability. LINEAR’s pattern of sky coverage produces repeat photometry data for stars on several timescales ranging from the 15–20 minute interval between images within a frameset, to a few days between repeat visits during one lunation, to the month-long timescale between lunar months, to the yearly.

## APPENDIX B

### LINEAR DATABASE SCHEMA

The LINEAR database hosted at SkyDOT contains two tables, “Object” and “Source.” The “Source” table contains photometry and astrometry of individual LINEAR detections (sources), while the “Object” table references time series obtained by clustering sources within  $2''$ . In addition, the “Object” table contains various low-level statistics calculated on time series and is cross-matched to external catalogs such as SDSS and Two Micron All Sky Survey (Skrutskie et al. 2006). A detailed description of various parameters provided by these tables is given in Tables 1 and 2, and a screenshot showing the SkyDOT interface is shown in Figure 17.

**Table 1**  
LINEAR “Source” Table Schema

Field	Description
sourceID	A unique number identifying this source
ra	Equatorial J2000.0 right ascension
decl	Equatorial J2000.0 declination
MJD	Modified Julian Date
mag	Recalibrated LINEAR magnitude
magErr	Uncertainty in the recalibrated LINEAR magnitude
calib	1 if the source was used for calibration, 0 otherwise
ellip	“Ellipticity” parameter measured by SExtractor
ximg	Position of the source along CCD’s $x$ -axis
yimg	Position of the source along CCD’s $y$ -axis
FWHM	FWHM measured by SExtractor
flags <sup>a</sup>	SExtractor internal flags
objectID	A number associating this source with an object in the “Object” table

**Note.** <sup>a</sup> See p. 28 in the SExtractor manual (<https://www.astromatic.net/pubsvn/software/sextractor/trunk/doc/sextractor.pdf>).



**Table 2**  
LINEAR “Object” Table Schema

Field	Description
objectID	A unique number identifying this object
ra	Mean equatorial J2000.0 right ascension
decl	Mean equatorial J2000.0 declination
ra_std	rms scatter in right ascension (in units of arcsec)
decl_std	rms scatter in declination (in units of arcsec)
ra_median	Median equatorial J2000.0 right ascension
decl_median	Median equatorial J2000.0 declination
nptsTotal	Number of detections
nptsGood	Number of detections with flag==0
mag_mean	Mean recalibrated LINEAR magnitude
mag_wmean	Weighted recalibrated LINEAR magnitude (by magnitude errors)
mag_median	Median recalibrated LINEAR magnitude
mag_std	rms scatter of recalibrated LINEAR magnitudes
mag_wstd	Weighted rms scatter of recalibrated LINEAR magnitudes (by magnitude errors)
mag_skew	Skewness of recalibrated LINEAR magnitudes
mag_kurtosis	Kurtosis of recalibrated LINEAR magnitudes
mag_chi2dof	$\chi^2$ per degree of freedom around the mean magnitude
mag_rchi2dof <sup>a</sup>	Robust $\chi^2$ per degree of freedom around the mean magnitude
theta_sdss <sup>b</sup>	Distance in arcsec from the SDSS source
sdssID	SDSS Data Release 7 objID parameter
sdss_ra	SDSS J2000.0 right ascension
sdss_dec	SDSS J2000.0 declination
objtype	6 if unresolved in SDSS imaging (i.e., a point source), 3 if resolved
rExt	Extinction in the SDSS <i>r</i> -band
uMod	SDSS <i>u</i> -band model magnitude
gMod	SDSS <i>g</i> -band model magnitude
rMod	SDSS <i>r</i> -band model magnitude
iMod	SDSS <i>i</i> -band model magnitude
zMod	SDSS <i>z</i> -band model magnitude
uErr	SDSS <i>u</i> -band model magnitude error
gErr	SDSS <i>g</i> -band model magnitude error
rErr	SDSS <i>r</i> -band model magnitude error
iErr	SDSS <i>i</i> -band model magnitude error
zErr	SDSS <i>z</i> -band model magnitude error
ug	SDSS <i>u</i> – <i>g</i> color (corrected for ISM extinction, $u - g = (uMod - 1.87rExt) - (gMod - 1.38rExt)$ )
gr	SDSS <i>g</i> – <i>r</i> color (corrected for ISM extinction, $g - r = (gMod - 1.38rExt) - (rMod - 1.00rExt)$ )
ri	SDSS <i>r</i> – <i>i</i> color (corrected for ISM extinction, $r - i = (rMod - 1.00rExt) - (iMod - 0.76rExt)$ )
iz	SDSS <i>i</i> – <i>z</i> color (corrected for ISM extinction, $i - z = (iMod - 0.76rExt) - (zMod - 0.54rExt)$ )
gi	SDSS <i>g</i> – <i>i</i> color (corrected for ISM extinction, $g - i = (gMod - 1.38rExt) - (iMod - 0.76rExt)$ )
pmL <sup>c</sup>	Proper motion in the Galactic latitude direction (in units of mas yr <sup>-1</sup> )
pmB <sup>c</sup>	Proper motion in the Galactic longitude direction (in units of mas yr <sup>-1</sup> )
pmErr <sup>c</sup>	Proper motion error (in units of mas yr <sup>-1</sup> )
isolated	1 if SDSS CHILD flag is set to 0 (isolated == 0 may indicate a close neighbor)
sdss_satur	1 if SDSS SATURATED flag is set to 1
sdss_flags	SDSS flags encoded as a 64-bit integer number
theta_2mass <sup>d</sup>	Distance in arcsec from the 2MASS source
J	2MASS <i>J</i> -band magnitude
JErr	2MASS <i>J</i> -band magnitude error
H	2MASS <i>H</i> -band magnitude
HErr	2MASS <i>H</i> -band magnitude error
K	2MASS <i>K</i> -band magnitude
KErr	2MASS <i>K</i> -band magnitude error
jh	2MASS <i>J</i> – <i>H</i> color (corrected for extinction, $j - h = (J - 0.327rExt) - (H - 0.209rExt)$ )
hk	2MASS <i>H</i> – <i>K</i> color (corrected for extinction, $h - k = (H - 0.209rExt) - (K - 0.133rExt)$ )
jk	2MASS <i>J</i> – <i>K</i> color (corrected for extinction, $(J - 0.327rExt) - (K - 0.133rExt)$ )

**Notes.**

<sup>a</sup> Calculated after eliminating 10% of highest and 10% of lowest magnitudes.

<sup>b</sup> This and other SDSS parameters set to NULL if no match within 2'' and not in SDSS footprint, set to 100 if in SDSS footprint but no match within 2''.

<sup>c</sup> Obtained from the Munn et al. (2004) SDSS-USNOB proper motion catalog.

<sup>d</sup> This and other 2MASS parameters set to NULL if no match within 2''. Following Covey et al. (2007), we only match to 2MASS sources with the following 2MASS flags:  $rd_{\text{flag}} = 222$ ,  $bl_{\text{flag}} = 111$ , and  $cc_{\text{flag}} = 0$ .



**The LINEAR Survey Photometric Database**

Home SQL Query Object Search Catalog Matching Light Curves Documentation Contact WSGI Environment

Now Viewing: user\_sql\_query

SQL query

```
select * from source where "objectID" = 1030;
```

Output:

Your query: "select \* from source where "objectID" = 1030; "

Matching records

Item	sourceID	ra	decl	MJD	mag	magErr	calib	ellip
1	1634337	115.843476	65.736482	52636.3064595	14.07	0.01	0	0.025
2	3209021	115.843379	65.736453	52636.3498227	14.105	0.01	0	0.005
3	6385157	115.843423	65.736468	52636.3209077	14.077	0.01	0	0.035
4	6508400	115.843364	65.736455	52636.3353559	14.074	0.01	0	0.08
5	6815434	115.843422	65.736473	52636.2917809	14.069	0.01	0	0.058
6	10495189	115.843327	65.736382	52621.3346657	14.066	0.008	0	0.037

10 Page 1 of 19 Displaying 1 to 10 of 186 items

TURBOGEARS G Przemek Wozniak, Copyright (c) 2011

**Figure 17.** Screenshot showing the search interface for the LINEAR database.  
(A color version of this figure is available in the online journal.)

## REFERENCES

- Abazajian, K., Adelman-McCarthy, J. K., Agüeros, M. A., et al. 2009, *ApJS*, **182**, 543
- Akerlof, C., Amrose, S., Balsano, R., et al. 2000, *AJ*, **119**, 1901
- Andersen, J. 1991, *A&AR*, **3**, 91
- Ankerst, M., Breuning, M. M., Kriegel, H.-P., & Sander, J. 1999, Proc. 1999 ACM SIGMOD International Conf. on Management of Data, ed. S. B. Davidson & C. Faloutsos, 49
- Barron, J. T., Hogg, D. W., Lang, D., & Roweis, S. 2008, *AJ*, **136**, 1490
- Becker, A. C., Wittman, D. M., Boeshaar, P. C., et al. 2004, *ApJ*, **611**, 418
- Bertin, E., & Arnouts, S. 1996, *A&AS*, **117**, 393
- Burke, B., Gregory, J. A., Mountain, R. W., et al. 1998, *Exp. Astron.*, **8**, 31
- Covey, K. R., Ivezić, Ž., Schlegel, D., et al. 2007, *AJ*, **134**, 2398
- Guinan, E. F., Fitzpatrick, E. L., Dewarf, L. E., et al. 1998, *ApJ*, **509**, L21
- Ivezić, Ž., Tyson, J. A., Acosta, E., et al. 2008, arXiv:0805.2366
- Kaiser, N., Aussel, H., Burke, B. E., et al. 2002, Proc. SPIE, **4836**, 154
- Lang, D., Hogg, D. W., Mierle, K., Blanton, M., & Roweis, S. 2010, *AJ*, **139**, 1782
- Law, N. M., Kulkarni, S. R., Dekany, R. G., et al. 2009, *PASP*, **121**, 1395
- Lupton, R. H., Ivezić, Ž., Gunn, J. E., et al. 2002, Proc. SPIE, **4836**, 350
- Miceli, A., Rest, A., Stubbs, C. W., et al. 2008, *ApJ*, **678**, 865
- Monet, D. G., Levine, S. E., Canzian, B., et al. 2003, *AJ*, **125**, 984
- Munn, J. A., Monet, D. G., Levine, S. E., et al. 2004, *AJ*, **127**, 3034
- Pier, J. R., Munn, J. A., Hindsley, R. B., et al. 2003, *AJ*, **125**, 1559
- Pojmański, G. 2002, *Acta Astron.*, **52**, 397
- Prša, A., & Zwitter, T. 2005, *ApJ*, **628**, 426
- Rau, A., Kulkarni, S. R., Law, N. M., et al. 2009, *PASP*, **121**, 1334
- Reimann, J. D. 1994, PhD thesis, Univ. California
- Sesar, B., Ivezić, Ž., Lupton, R. H., et al. 2007, *AJ*, **134**, 2236
- Sesar, B., Svilković, D., Ivezić, Ž., et al. 2006, *AJ*, **131**, 2801
- Skrutskie, M. F., Cutri, R. M., Stiening, R., et al. 2006, *AJ*, **131**, 1163
- Stokes, G., Evans, J. B., Viggh, H. E. M., Shelly, F. C., & Pearce, E. C. 2000, *Icarus*, **148**, 21
- Torres, G., Andersen, J., & Giménez, A. 2010, *A&AR*, **18**, 67
- Woźniak, P. R., Vestrand, W. T., Akerlof, C. W., et al. 2004, *AJ*, **127**, 2436
- York, D. G., Adelman, J., Anderson, J. E., Jr., et al. 2000, *AJ*, **120**, 1579